Supporting Information

Ultra-multi-mode high-Q plasmonic resonances by extracting guided modes via metallic lattice

Limin Lin, Shuang Qiu, Xuanyi Liu, Zuhai Ma, Mengran Jiang, Jiancai Xue, and Zhang-Kai Zhou**

1. Lorentzian Linear Fitting and Q-factor Calculation

This involves fitting experimental data to a Lorentzian function. The Lorentzian line-shape is characterized by

$$R(\lambda) = R_0 + \frac{A}{1+(\frac{2(\lambda-\lambda_0)}{\gamma})^2} \qquad (1)$$

where: λ_0 is the resonance frequency, γ is the full width at half maximum (FWHM), A is the amplitude.

The quality factor (Q-factor) quantifies the sharpness of a resonance and is defined as

$$Q = \frac{\lambda_0}{\gamma} \qquad (2)$$

2. Theoretical data of TE modes

Table S1. Wavelengths of eigenvalue TE modes and their corresponding *N* values

Lambda of TE modes (nm)	***N*, the integer in formula (1)**
886.2	0
880.7	1
871.8	2
859.8	3
845.0	4
827.9	5
809.0	6
788.7	7
767.5	8
745.6	9
723.5	10
701.4	11
679.6	12
658.1	13
637.3	14
617.2	15

3. Calculated mode volume

Mode volume is calculated by using the following formula[1]:

$$V_m = \frac{\int \varepsilon_{eff}(r)\left|E(r)\right|^2 d^3r}{\max[\varepsilon_{eff}(r)\left|E(r)\right|^2]} \tag{3}$$

$$\varepsilon_{eff}(r) = \mathrm{Re}\,\varepsilon(\mathrm{r},\omega) + \frac{2\omega \mathrm{Im}\,\varepsilon(r,\omega)}{\gamma} \tag{4}$$

where $|E(r)|^2$ is the electric field intensity at position *r*, $\varepsilon_{eff}(r)$ is the effective permittivity at position *r*, ω is the frequency.

As the Table S2 shown, the mode volumes of the modes in the presented nanostructure are comparable with that of the LSPR and SLR in the pristine plasmonic lattice, indicating that these modes possess excellent capability of field localization as strong as that of the plasmonic resonance modes of the pristine lattice.

Table S2. Mode volume of our structure and pristine plasmonic lattice

	Mode wavelength (nm)	Mode volume $(\frac{\lambda}{n})^3$
Pristine plasmonic lattice	691.0 (LSPR)	0.0250
	877.8 (SLR)	0.0156
Our structure	665.3	0.0221
	671.1	0.0114
	686.5	0.0283
	695.7	0.0165
	708.4	0.0120
	717.9	0.0069
	729.9	0.0098
	738.4	0.0066
	746.3	0.0162
	847.2	0.0407
	862.5	0.0528
	874.9	0.0325
	883.1	0.0293
	887.4	0.0411

4. Surface charge distribution.

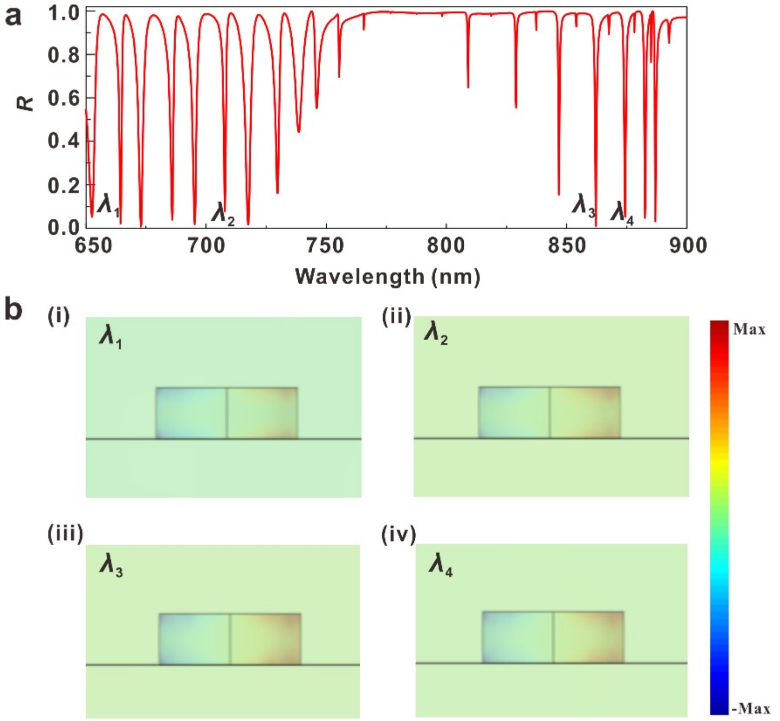

Figure S1: Simulated surface charge distribution of the Au nanostructure array using COMSOL Multiphysics. **(a)** The reflection spectrum of DMDM nanostructure. **(b)** Surface charge density of four modes selected arbitrarily from (a). The surface charge density ρ is represented by the normal component of the electric displacement field D, $\rho = D \cdot \hat{n}$, evaluated at the Au/air interface. The opposing sign of charges accumulated at opposite ends of the structure along the incident polarization direction (x-direction) confirms the excitation of a dipolar plasmonic resonance mode.

5. Normalized spatial mode overlap integral of DMDM.

To quantify the degree of spatial co-localization, we computed the normalized overlap integral for every pair of modes, the overlap coefficient is defined as

$$h_{\text{ij}} = \frac{\left| \iint E_i^* \cdot E_j dA \right|^2}{\iint \left| E_i \right|^2 dA \cdot \iint \left| E_j \right|^2 dA} \qquad (5)$$

where Ei and Ej are the complex electric field vector distributions of mode i and mode j, respectively; the asterisk denotes complex conjugation; the double integral is evaluated over the cross-sectional area A of the structure. The denominator normalizes the integral by the individual field energies of each mode, ensuring that $\eta_{ij}\,\epsilon$ [0, 1], where unity indicates identical spatial distributions and zero indicates complete orthogonality.

The integration is performed over the xy cross-section at the upper surface of the Au disk where the field enhancement is most pronounced as shown in Fig.S6. The resulting 14×14 overlap matrix is presented in Figure S2. Taken together, the field distribution images and the quantitative overlap matrix demonstrate that all resonant modes supported by the structure are spatially co-localized at the Au disk periphery. The high intra-group overlap values (up to 0.998) provide direct quantitative evidence for the "excellent spatial mode overlap" claimed in the manuscript, and the non-zero cross-group overlap confirms that inter-group interaction is spatially permitted.

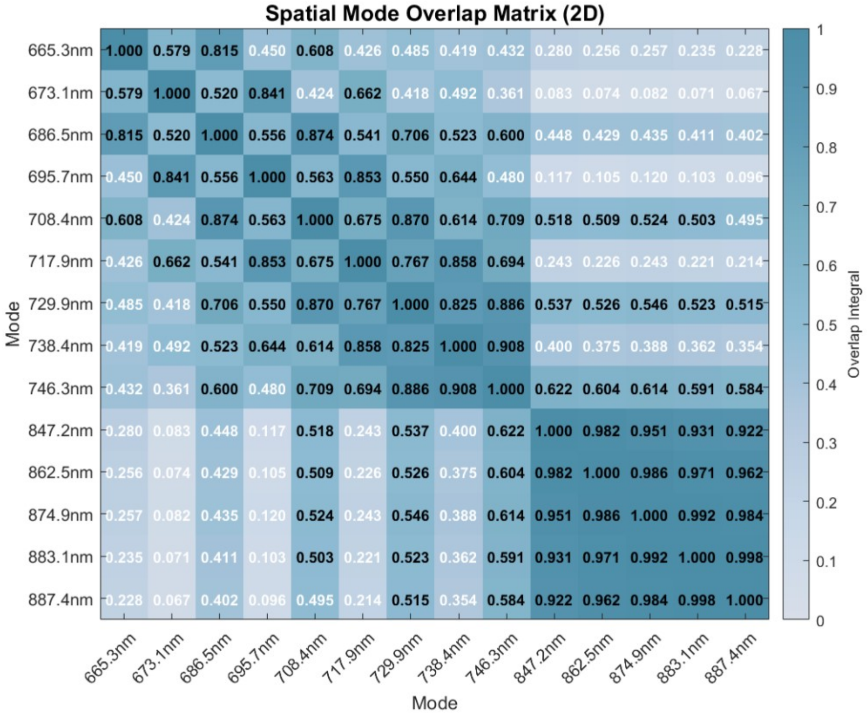

	665.3nm	673.1nm	686.5nm	695.7nm	708.4nm	717.9nm	729.9nm	738.4nm	746.3nm	847.2nm	862.5nm	874.9nm	883.1nm	887.4nm
665.3nm	1.000	0.579	0.815	0.450	0.608	0.426	0.485	0.419	0.432	0.280	0.256	0.257	0.235	0.228
673.1nm	0.579	1.000	0.520	0.841	0.424	0.662	0.418	0.492	0.361	0.083	0.074	0.082	0.071	0.067
686.5nm	0.815	0.520	1.000	0.556	0.874	0.541	0.706	0.523	0.600	0.448	0.429	0.435	0.411	0.402
695.7nm	0.450	0.841	0.556	1.000	0.563	0.853	0.550	0.644	0.480	0.117	0.105	0.120	0.103	0.096
708.4nm	0.608	0.424	0.874	0.563	1.000	0.675	0.870	0.614	0.709	0.518	0.509	0.524	0.503	0.495
717.9nm	0.426	0.662	0.541	0.853	0.675	1.000	0.767	0.858	0.694	0.243	0.226	0.243	0.221	0.214
729.9nm	0.485	0.418	0.706	0.550	0.870	0.767	1.000	0.825	0.886	0.537	0.526	0.546	0.523	0.515
738.4nm	0.419	0.492	0.523	0.644	0.614	0.858	0.825	1.000	0.908	0.400	0.375	0.388	0.362	0.354
746.3nm	0.432	0.361	0.600	0.480	0.709	0.694	0.886	0.908	1.000	0.622	0.604	0.614	0.591	0.584
847.2nm	0.280	0.083	0.448	0.117	0.518	0.243	0.537	0.400	0.622	1.000	0.982	0.951	0.931	0.922
862.5nm	0.256	0.074	0.429	0.105	0.509	0.226	0.526	0.375	0.604	0.982	1.000	0.986	0.971	0.962
874.9nm	0.257	0.082	0.435	0.120	0.524	0.243	0.546	0.388	0.614	0.951	0.986	1.000	0.992	0.984
883.1nm	0.235	0.071	0.411	0.103	0.503	0.221	0.523	0.362	0.591	0.931	0.971	0.992	1.000	0.998
887.4nm	0.228	0.067	0.402	0.096	0.495	0.214	0.515	0.354	0.584	0.922	0.962	0.984	0.998	1.000

Figure S2: Normalized spatial modes overlap integral of DMDM.

6. E_x distribution of eigenvalue TE modes.

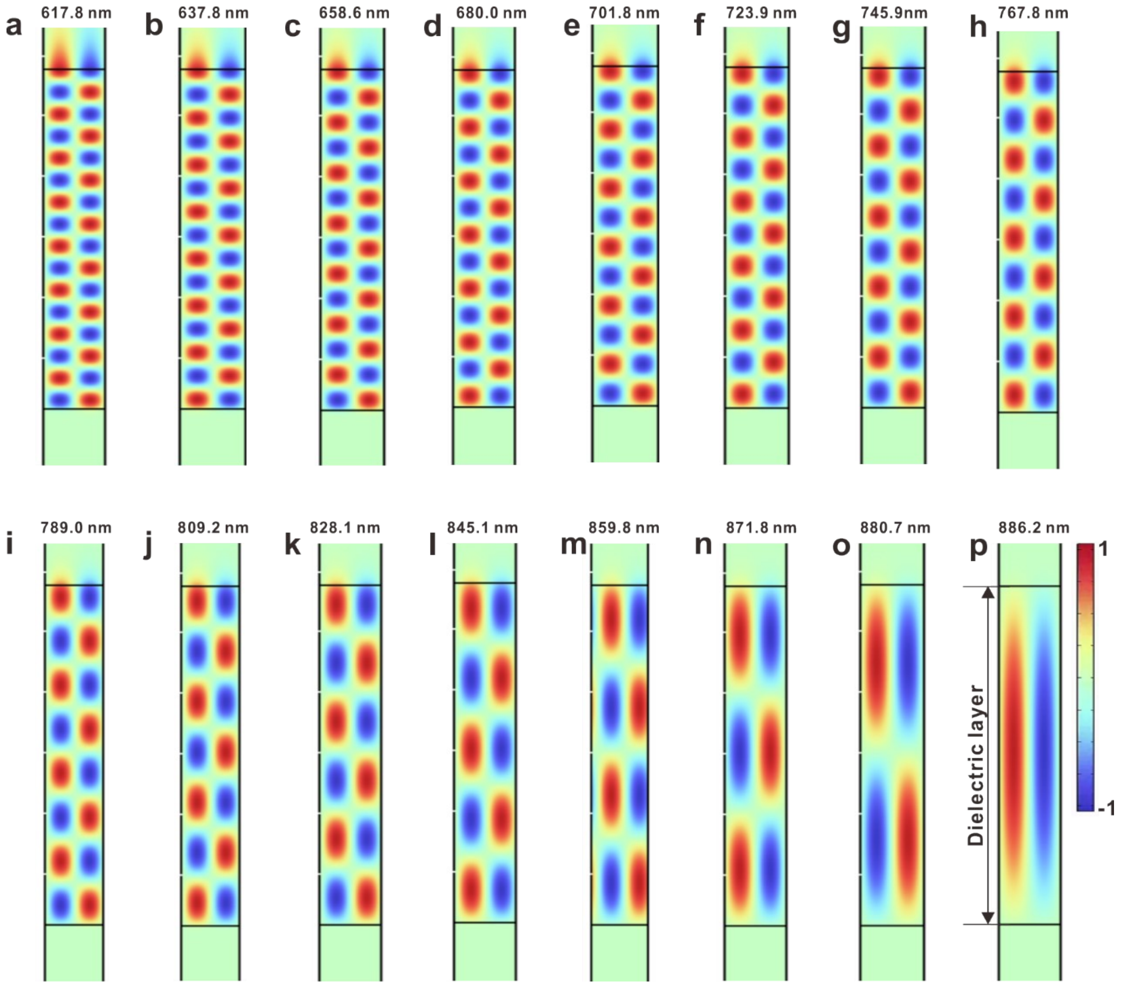

Figure S3. All diagrams are E_x distribution of eigenvalue TE GMs with various N showing the anti-symmetric feature along the propagation direction of the GMs. All diagrams were set in same scale.

7. *H* distribution of eigenvalue TE modes.

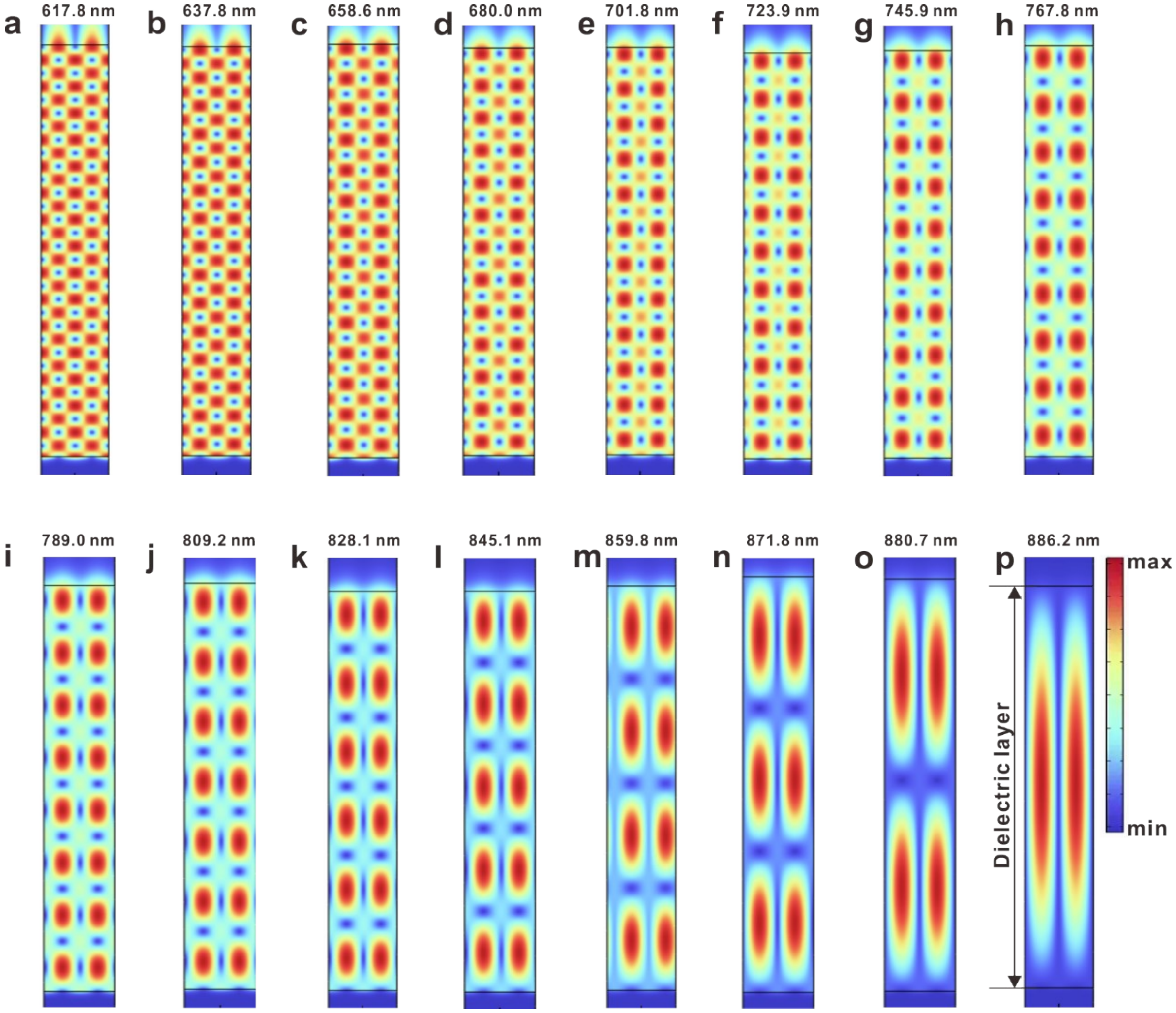

Figure S4. All diagrams are *H* distribution of eigenvalue TE GMs with various *N*.

8. TM modes in a multilayer system (air/dielectric/Ag layers).

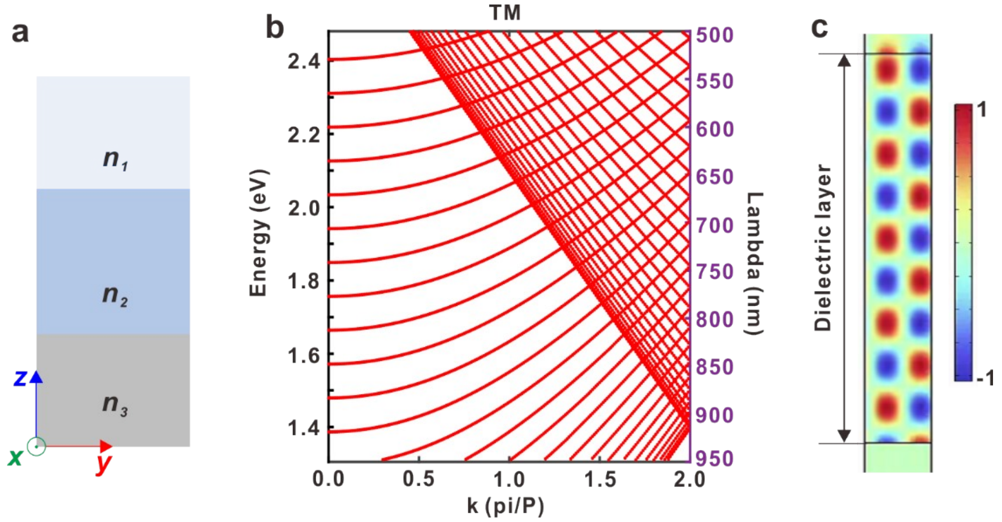

Figure S5: TM modes in a multilayer system (air/dielectric/Ag layers). **(a)** schematic of a three-layer thin-film waveguide. **(b)** Dispersion relationship of TM modes. **(c)** Simulated E_z distribution of guide mode TM_{18} at 756.9 nm in *y*-*z* plane.

9. More electric field enhancements of the multiple high-Q mode as show in Figure 3a.

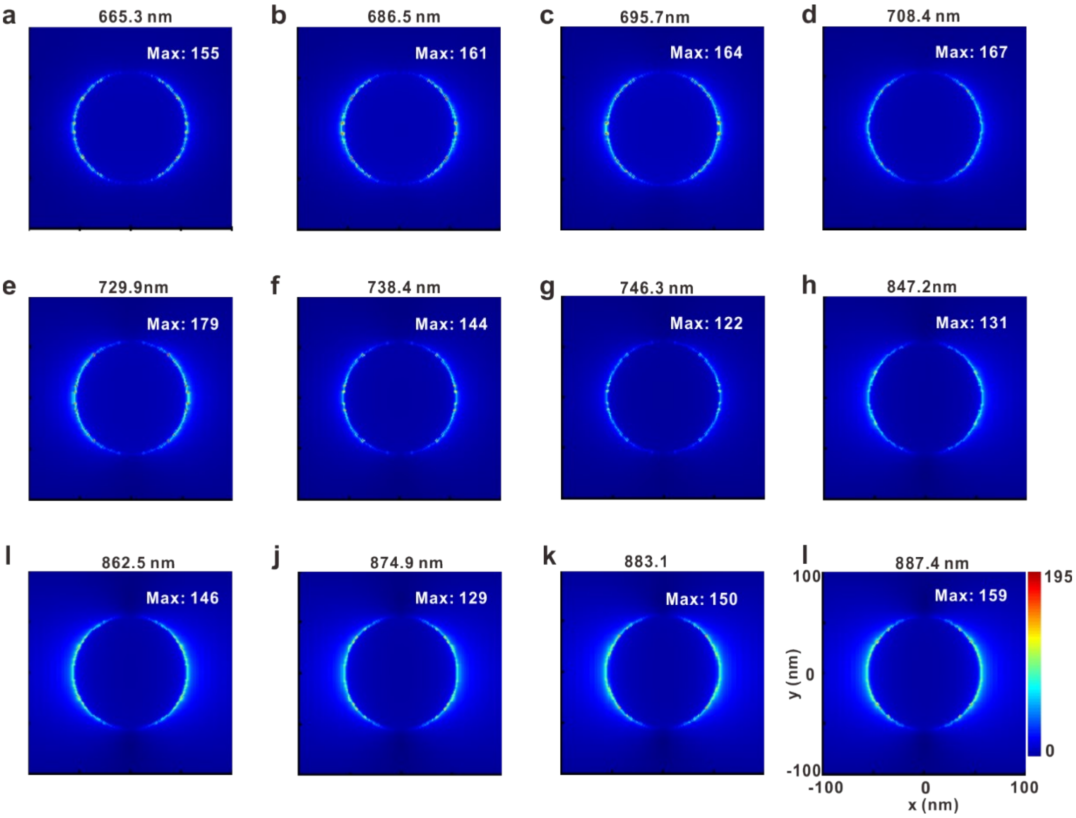

Figure S6: (a-l) Electric field enhancements in x-y plane at various wavelengths. All the electric field enhancements were set in same scale and axis as Figure 3a.

10. Robustness of refractive index matching.

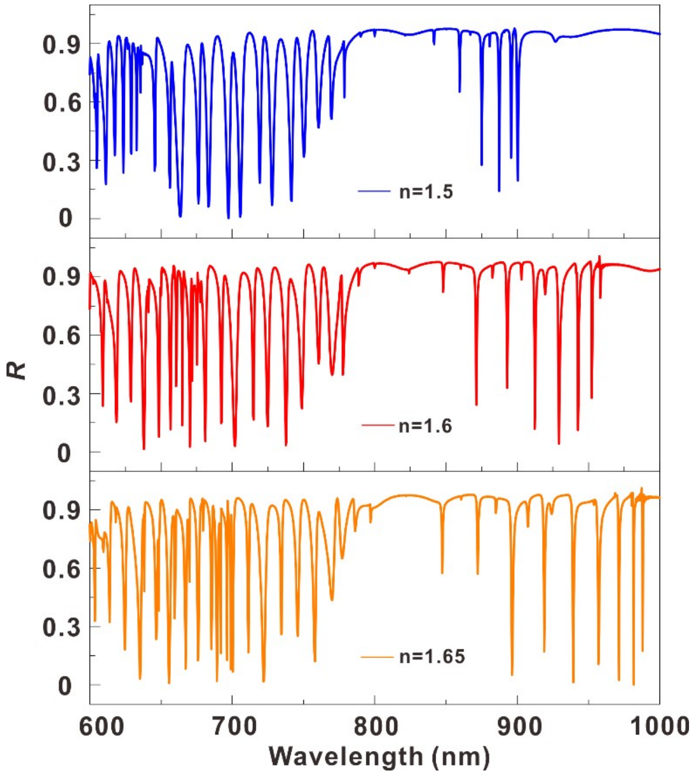

Figure S7: Reflection spectra under different refractive index conditions. It should be specifically noted that *n* here refers to the refractive index of the upper dielectric layer of the Au array in the DMDM structure. As *n* increases, the refractive indices of the upper and lower dielectric layers of the Au array are no longer matched, the mode does not gradually disappear due to this refractive index mismatch. This also demonstrates that the structure possesses good robustness.

11. Simulated phases of the magnetic field components in the z-direction

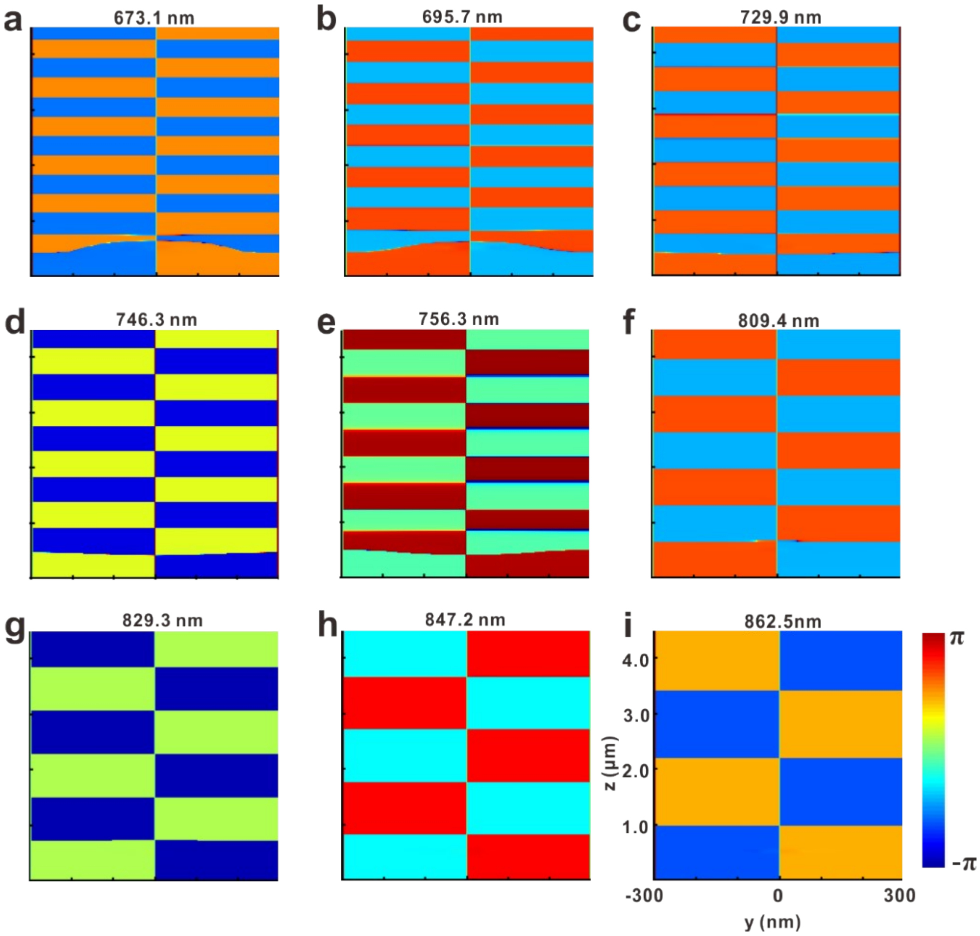

Figure S8: Simulated phases of the magnetic field components in the z-direction (H_z) at **(a)** 673.1 nm, **(b)** 695.7 nm, **(c)** 729.9 nm, **(d)** 746.3 nm, **(e)** 756.3 nm, **(f)** 809.4 nm, **(g)** 829.3 nm, **(h)** 847.2 nm, and **(i)** 862.5 nm. All the diagrams were set in same scale and axis.

12. Simulated magnetic field components in the z-direction of DMDM.

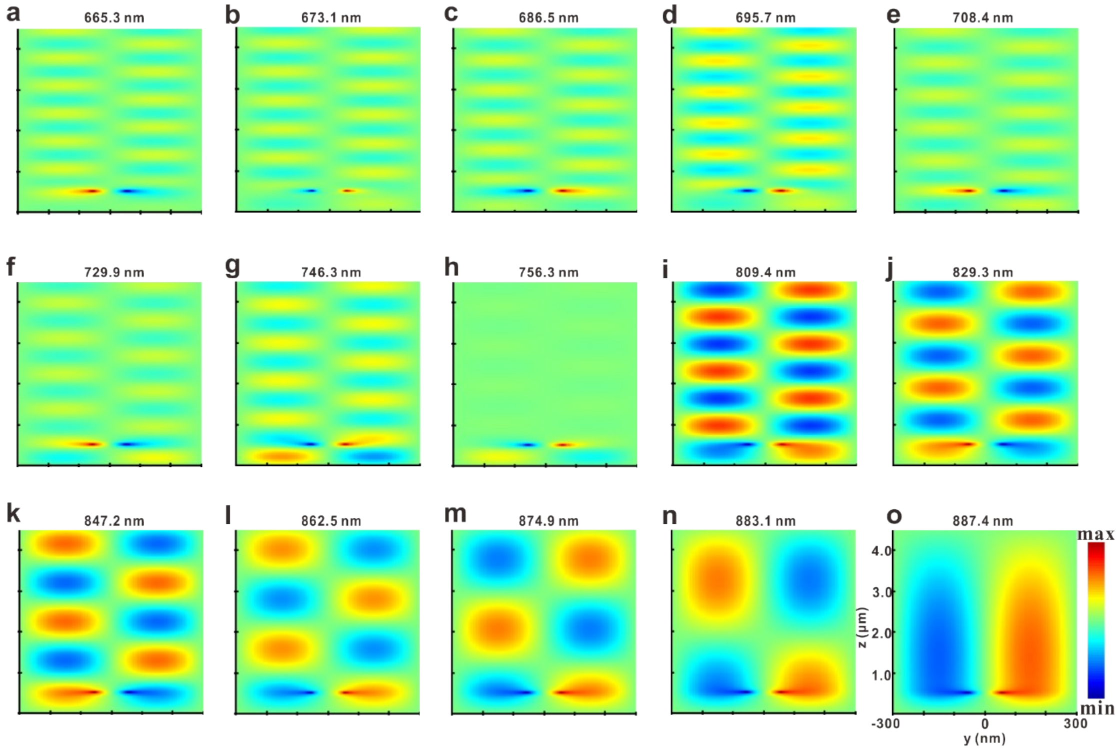

Figure S9. Simulated magnetic field components at various wavelengths in the z-direction (H_z) of the DMDM. All diagrams were set in same scale and axis.

13. Angle-resolved spectroscopy of the DMDM.

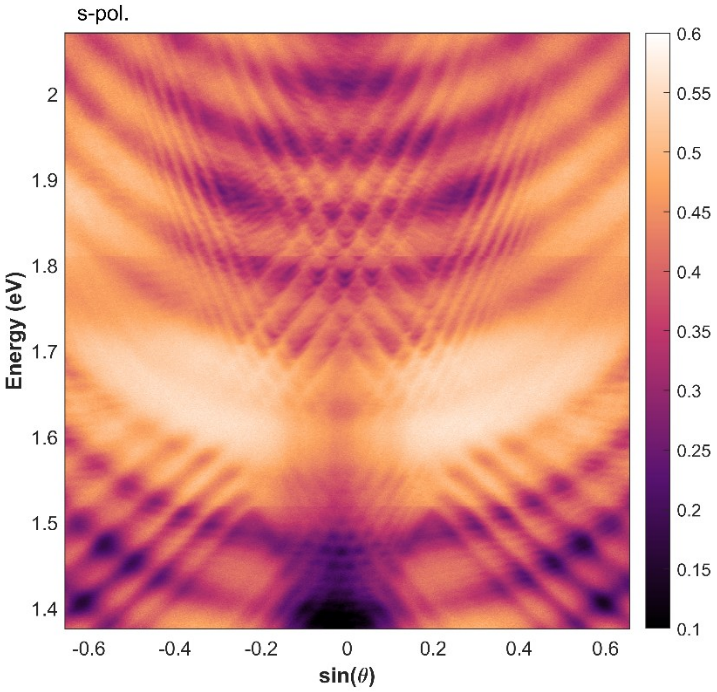

Figure S10: The dispersion features of the DMDM are examined by angle-resolved spectroscopy under s polarization. The angle-resolved spectroscopy was measured by ARMS, Angle-Resolved Micro-Spectrometer, ideaoptics, China.

14. Experiment reflection spectrum

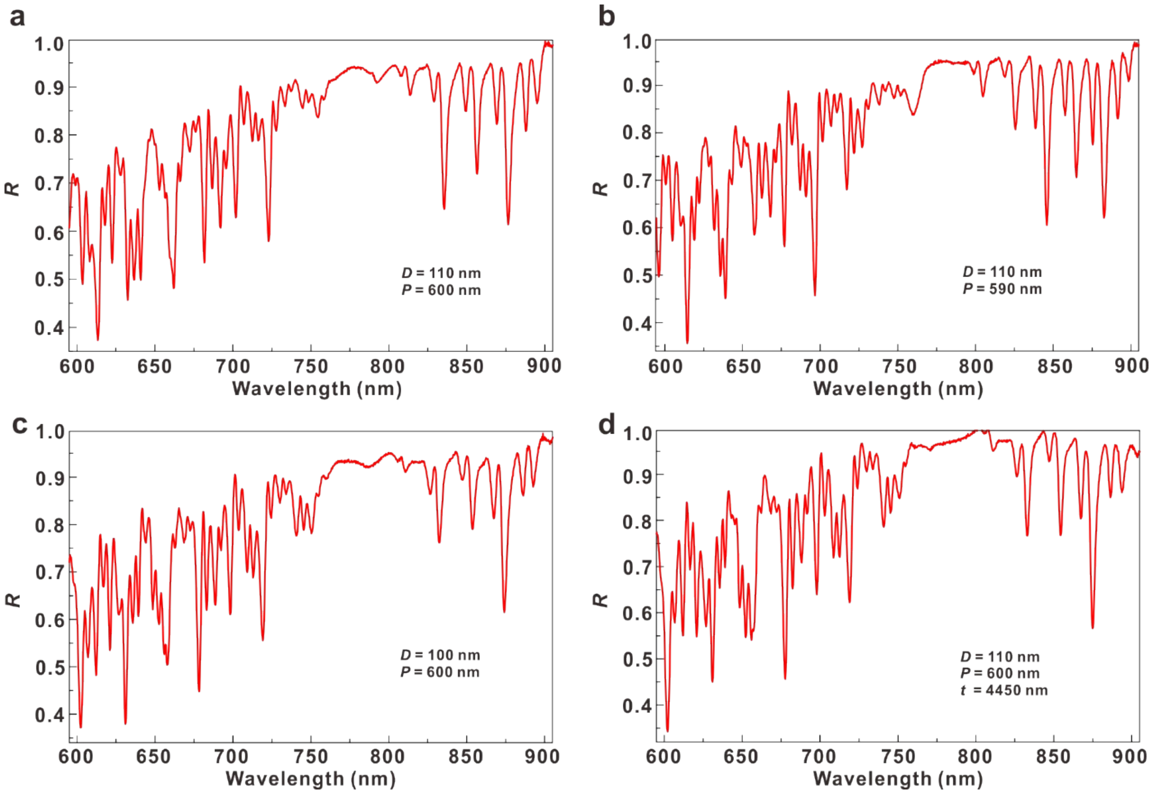

Figure S11. **(a)** The wide-band reflection spectra of the sample characterized as Figure 4c and 4d with *D* = 110 nm, *P* = 600 nm, and *t* = 4500 nm. **(b-d)** The reflection spectrums correspond to the Q factor shown in Figure 4e with (b) *D* = 110 nm, *P* = 590 nm, *t* = 4500nm, (c) *D* = 100 nm, *P* = 600 nm, *t* = 4500nm, (d) *D* = 110 nm, *P* = 600 nm, *t* = 4450nm. By changing the period of the nanoarray *P*, the diameter *D* of the nanoparticles, and the thickness of the dielectric layer *t*, the modes of the DMDM can be modulated with relatively high Q factors.

15. Experiment results of polarization-dependent modulation.

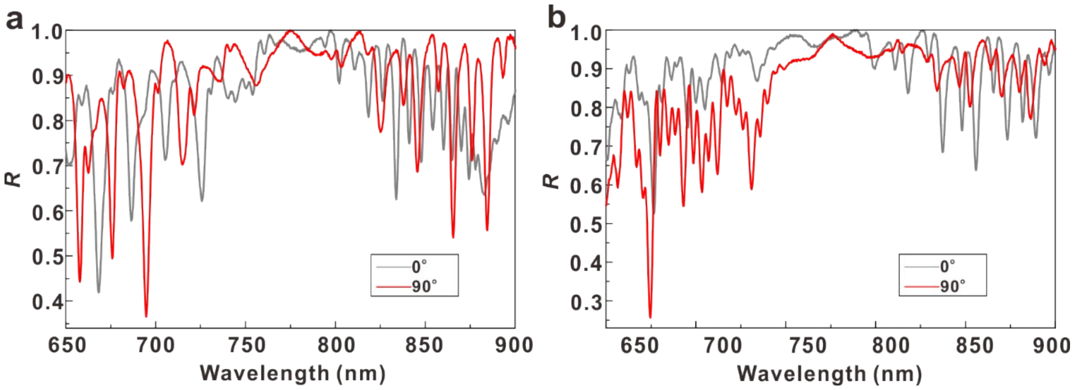

Figure S12: (a-b) The original experiment reflection spectra of Figure 5 (c) and (f) excited by 0° (x) and 90° (y) polarizations. (a) The structural parameters are $D = 120$ nm, $H = 40$ nm, $t = 4500$ nm, $P_x = 600$ nm, $P_y = 560$ nm. (b) The structural parameters are $P = 590$ nm, $H = 40$ nm, $t = 4500$ nm, the diameters in x direction $a = 130$ nm, in y direction $b = 80$ nm.

16. Spectrum with different ratio of short axis to long axis *b/a*.

For the anisotropic nanodisk geometry, the spectral response is inherently polarization-dependent. Under 0°-polarized excitation, the resonance characteristics are predominantly governed by the *a* and the lattice period along that direction (*Px*), which collectively determine the localized surface plasmon resonance (LSPR) and the surface lattice resonance (SLR) conditions. Conversely, under 90°-polarized excitation, the LSPR and SLR are primarily dictated by the *b* and the corresponding lattice period (*Py*), which in turn shapes the overall spectral response. As shown in Fig.S13, when increasing *b* and keeping *a* constant, the optical response shows slight change in Fig.S13a, but a progressive red-shift of the resonance positions in Fig.S13(b).

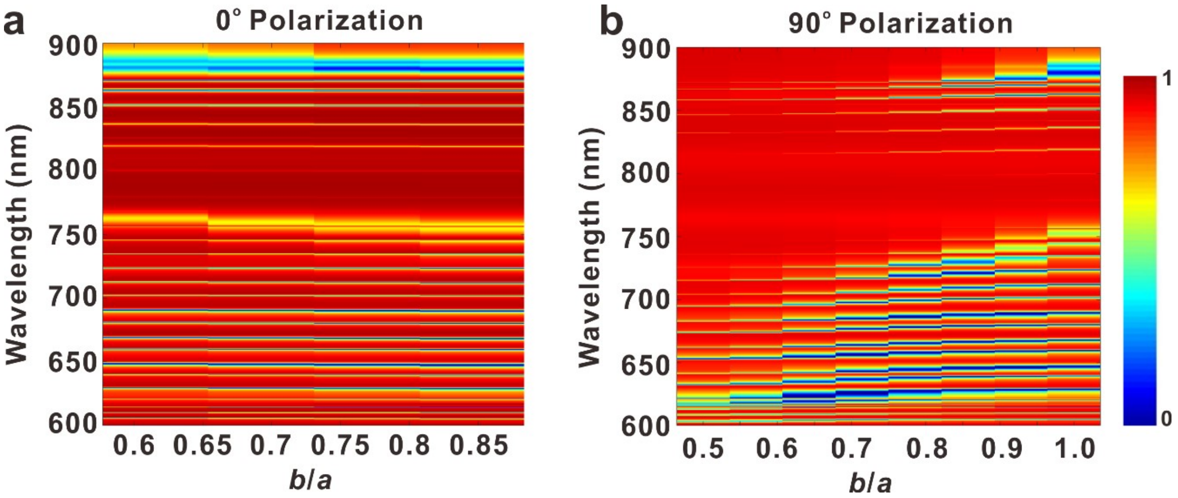

Figure S13. Spectra with different ratio of short axis to long axis *b/a*. (a-b) The reflectance spectrum excited by 0° and 90° polarizations. Parameters of the structure are $P = 590$ nm, $H = 40$ nm, $t = 4500$ nm, and the diameter in x direction $a = 130$ nm. The diameter in y direction b increased from 65nm to 130 nm (a), and 80 nm to 120 nm (b).

References

1 Koenderink AF. On the use of Purcell factors for plasmon antennas. Opt Lett. 2010;35:24.